Coherent reconstruction of pump beams through recombination of entangled photon pairs

G. Daniel Jimenez,[1] Veneranda G. Garces,[2] and Kevin A. O'Donnell[1,2,*]

[1]*División de Física Aplicada, Centro de Investigación Científica y de Educación Superior de Ensenada, Carretera Ensenada-Tijuana No. 3918, Zona Playitas, C.P. 22860, Ensenada, Baja California, Mexico*

[2]*Pacifica Photonics Consultants, Carretera Tijuana-Ensenada No. 7165, El Sauzal, C.P. 22760, Ensenada, Baja California, Mexico*

(Received 29 July 2018; revised manuscript received 15 October 2018; published 26 February 2019)

In theoretical and experimental work, we consider the process in which an entangled photon pair recombines into a single photon in a nonlinear crystal, with particular interest in the amplitude distribution and coherence properties of the up-converted light. It is found that the up-converted state has perfect mutual coherence with the pump that originally produced the photon pair in another nonlinear crystal and that the amplitude has the spatiotemporal structure of the original pump mode, filtered by a linear transfer function. These conclusions are drawn from leading-order calculations performed in the interaction picture, with the multimodal nature of all fields being fully accounted for. In our experimental results, we observe the spatial similarity between the up-converted light and the original pump mode; their mutual coherence is demonstrated through observation of fringes with near-unit visibility. The effects studied here have potential applications in quantum information processing and also confirm that the principle of path indistinguishability holds even under unusually extreme conditions.

DOI: 10.1103/PhysRevA.99.023853

I. INTRODUCTION

While the entangled photon pairs produced by spontaneous parametric down-conversion (SPDC) have been widely studied, the novel effects that arise using two nonlinear crystals have attracted particular interest. If the two crystals are coherently pumped, it has been shown that introducing the idler photons of the SPDC from one crystal into another induces coherence between the signal photons of the two crystals [1,2]. Further, overlapping the SPDC cones produced by two crystals has been found to produce interference fringes in the detected photon pair rates, whose phase depends on the pump phase difference between the two crystals [3–5]. More recently, extensions of such experiments have been of interest [6–9], while other works have been developing applications for these effects [10–14]. From a physical point of view, despite the lack of second-order amplitude coherence between the signal and idler modes [15], it is well known that the SPDC quantum state still carries information about the pump phase [3–5].

Here, in both theoretical and experimental work, we consider a different situation in which similar effects appear. We also employ two nonlinear crystals, although only the first crystal is pumped to produce photon pairs. The pump beam is then removed and, after dispersion compensation, the SPDC emission cone is focused in the second crystal. There, an entangled photon pair can recombine into a single photon that, from energy conservation, has the same frequency as the pump photon that produced the pair. These effects have been observed using periodically poled crystals [16–20], which is our interest here, as well as using nonlinear waveguides [21–23]; however, such prior work has not considered the effects to be described here. Fully accounting for the multimodal quantum nature of all interacting states, we calculate the up-converted quantum state to first order in the interaction picture and consider its mutual coherence with the original pump light. In our experiments, we observe the spatial structure of the up-converted light and also its interference with the pump. The detected photon rates are low ($\sim 10^3$ s^{-1}) but are adequate for such work.

As is consistent with our theoretical predictions, we observe interference fringes that demonstrate essentially perfect mutual coherence between the up-converted light and attenuated pump light. Limited by mechanical and thermal experimental stability, the observed fringes are stable for tens of seconds, which is ∼8 and ∼15 orders of magnitude longer than the reciprocal of the pump and SPDC bandwidths, respectively. Moreover, the observed spatial structure of the up-converted light is found to strongly resemble the original pump mode. This observation agrees with our theoretical development, where it is demonstrated that the up-converted amplitude distribution is related to the pump modal amplitude by a linear, *coherent* transfer function. Thus our approach may be considered to be a coherent form of quantum imaging [24] even though, of course, the only link between the input and output of our optical system is provided by the photon pair and vacuum terms of SPDC. Our results thus imply far more than simply a dependence on pump phase; in particular, even though it has long been established that SPDC contains information about the pump [15,25,26], we show that the pump amplitude distribution may, with a known fidelity, be *extracted from* the SPDC through pair recombination.

*pacificaphotonics@startmail.com

II. THEORY

A. State derivation

Here we develop an expression for the quantum state of the up-converted light produced at the output of a nonlinear crystal illuminated by SPDC. Related theoretical studies have appeared previously [27,28], although these works have employed single-spatial-mode analyses with all interacting waves assumed to be collinear. Another work [18] has made single-mode assumptions about the pump and up-converted states, while considering only the SPDC to be multimodal. Here we take a more physically realistic approach, using fully multimodal spatiotemporal representations throughout the analysis; such an approach is necessary to accurately represent the up-converted state, the wide range of wave vectors present in SPDC, and the pump beam shape in the crystal producing the SPDC. A second aspect of our approach is that we represent *all* of these interacting fields as fully quantum fields, which later allows us to rigorously determine the degree of mutual coherence between the pump and up-converted light. The development requires few simplifying assumptions, and we will also discuss application of the approach to experimental situations.

We start with the representation of the down-converted state that follows from first-order perturbation theory, which is derived in the Appendix. The pump beam is assumed to be directed along the z axis. We let $\mathbf{k}_\epsilon$ and ω_ϵ denote, respectively, the wave vectors and frequencies of the pump ($\epsilon = p$), signal ($\epsilon = s$), and idler waves ($\epsilon = i$) in the crystal. Further, $n_\epsilon \equiv n(\omega_\epsilon)$ and $\eta_\epsilon \equiv \eta(\omega_\epsilon)$ denote, respectively, the refractive index and the reciprocal of the group velocity of mode ϵ. The down-converted state in the SPDC crystal may be written in the form

$$|\psi_{\mathrm{SPDC}}\rangle = \left[\hat{I} - \int_{\mathcal{D}_s} d\mathbf{k}_s \int_{\mathcal{D}_i} d\mathbf{k}_i \psi(\mathbf{k}_s, \mathbf{k}_i)\hat{a}^\dagger(\mathbf{k}_s)\hat{a}^\dagger(\mathbf{k}_i)\right]|\mathrm{vac}\rangle, \tag{1}$$

where $\hat{I}$ is the identity operator and $\hat{a}^\dagger(\mathbf{k}_\epsilon)$ is the creation operator of mode ϵ, which operates on the vacuum. The integration domains $\mathcal{D}_s$ and $\mathcal{D}_i$ are, respectively, the ranges of signal and idler wave vectors that are relevant, as described later. The two-photon amplitude $\psi(\mathbf{k}_s, \mathbf{k}_i)$ is given by [see Eq. (A11)]

$$\psi(\mathbf{k}_s, \mathbf{k}_i) = \sqrt{\frac{N_p d_{\mathrm{eff}}^2 L^2 \hbar(\omega_s+\omega_i)\omega_s\omega_i\eta_p^+}{16\pi^3\epsilon_0 c^3 n_p^+ n_s n_i \eta_s \eta_i}} \frac{\psi_p(\mathbf{k}_p^+)}{\cos\theta_p^{\mathrm{o}}} s\left(\Delta k_z^d\right) e^{i\Phi_p}, \tag{2}$$

where N_p is the mean number of pump photons in a time Δt long compared to the optical period, d_{eff} is the effective nonlinearity, L is the crystal length, $n_p^+ = n(\omega_s+\omega_i)$, $\eta_p^+ = \eta(\omega_s+\omega_i)$, $\psi_p(\mathbf{k}_p^+)$ is the pump amplitude, Φ_p is the pump phase, and $\mathbf{k}_p^+ = \mathbf{k}_p(\omega_s+\omega_i, \theta_p^{\mathrm{o}}, \phi_p^{\mathrm{o}})$ is directed at angles $(\theta_p^{\mathrm{o}}, \phi_p^{\mathrm{o}})$ in the crystal. Also, we assume that the crystal is periodically poled so that $\Delta\mathbf{k}^d = \mathbf{k}_p^+ - \mathbf{k}_s - \mathbf{k}_i - \mathbf{k}_g$ is the wave-vector mismatch, where $\mathbf{k}_g$ is the crystal poling wave vector, taken here as directed along the z axis. With Δk_z^d denoting the z component of $\Delta\mathbf{k}^d$, $s(\Delta k_z^d)$ is given by

$$s\left(\Delta k_z^d\right) = \frac{1}{L}\int_{-L/2}^{L/2} e^{i\Delta k_z^d z} dz = \mathrm{sinc}\left(\frac{\Delta k_z^d L}{2}\right). \tag{3}$$

The angles $(\theta_p^{\mathrm{o}}, \phi_p^{\mathrm{o}})$ may be found from a constraint that transverse components of $\Delta\mathbf{k}^d$ must be zero. This leads directly to the results

$$\tan\phi_p^{\mathrm{o}} = \frac{k_s \sin\theta_s \sin\phi_s + k_i \sin\theta_i \sin\phi_i}{k_s \sin\theta_s \cos\phi_s + k_i \sin\theta_i \cos\phi_i}, \tag{4}$$

$$\sin\theta_p^{\mathrm{o}} = \frac{k_s \sin\theta_s \cos\phi_s + k_i \sin\theta_i \cos\phi_i}{k_p^+ \cos\phi_p^{\mathrm{o}}}, \tag{5}$$

where $k_\epsilon = |\mathbf{k}_\epsilon| = n_\epsilon\omega_\epsilon/c$ and $(\theta_\epsilon, \phi_\epsilon)$ denote the angles of mode ϵ in the crystal.

We now consider the up-conversion of the SPDC in the second crystal. Here we make two assumptions: first, that the up-conversion crystal is optically identical to the SPDC crystal, and second, that its SPDC quantum state is identical to that produced within the SPDC crystal. The latter assumption requires an appropriate optical system to image the first crystal volume into the second crystal, as will be discussed in Sec. III A. The quantum state of the light produced by the up-conversion crystal is then calculated using first-order perturbation theory as [3,29,30]

$$|\psi_u\rangle = \left[\hat{I} - \frac{i}{\hbar}\int_{-\infty}^{\infty} dt\, \hat{H}_{\mathrm{int}}(t)\right]|\psi_{\mathrm{SPDC}}\rangle. \tag{6}$$

The interaction Hamiltonian for photon pair recombination is given by [25,31,32]

$$\hat{H}_{\mathrm{int}}(t) = 2\epsilon_0 \int d\boldsymbol{r}\, d(z)\hat{E}_p^{(-)}(\boldsymbol{r}, t)\hat{E}_s^{(+)}(\boldsymbol{r}, t)\hat{E}_i^{(+)}(\boldsymbol{r}, t) + \mathrm{H.c.}, \tag{7}$$

where the relevant term is written explicitly, H.c. denotes the Hermitian conjugate, and $d(z) = d_{\mathrm{eff}} e^{i\mathbf{k}_g\cdot\mathbf{r}}$ for first-order periodic poling [33]. The electric-field operators in Eq. (7) are written using a representation that describes fields with a continuous wave-vector spectrum within the dielectric as [34–36]

$$\hat{E}_\epsilon^{(+)}(\mathbf{r}, t) = i\int d\mathbf{k}_\epsilon \sqrt{\frac{\hbar\omega_\epsilon}{16\pi^3\epsilon_0 c n_\epsilon \eta_\epsilon}}\hat{a}(\mathbf{k}_\epsilon)e^{-i(\omega_\epsilon t - \mathbf{k}_\epsilon\cdot\mathbf{r})}, \tag{8}$$

where $\hat{E}_\epsilon^{(-)}(\mathbf{r}, t) = [\hat{E}_\epsilon^{(+)}(\mathbf{r}, t)]^\dagger$ and $\hat{a}(\mathbf{k}_\epsilon)$ is the annihilation operator of a mode with wave vector $\mathbf{k}_\epsilon$, which obeys the commutation relation $[\hat{a}(\mathbf{k}_\epsilon), \hat{a}^\dagger(\mathbf{k}'_\epsilon)] = \delta(\mathbf{k}_\epsilon - \mathbf{k}'_\epsilon)$.

We now substitute Eqs. (1), (2), (7), and (8) into Eq. (6). The temporal integration from Eq. (6) is performed and yields $2\pi\delta(\omega_p - \omega_s - \omega_i)$. The spatial integrations originating from Eq. (7) are done assuming that the transverse width of the crystal is large compared to the interaction region of the fields so that transverse integration limits are effectively infinite. This yields $(2\pi)^2 L\delta(\Delta k_x^u)\delta(\Delta k_y^u)s^*(\Delta k_z^u)$, where $\Delta\mathbf{k}^u = \mathbf{k}_p - \mathbf{k}_s - \mathbf{k}_i - \mathbf{k}_g$ is the wave-vector mismatch in the up-conversion crystal. After removing the photon pair state, we

have

$$|\psi_u\rangle = \left\{\hat{I} - \frac{\sqrt{N_p} d_{\rm eff}^2 L^2 \hbar}{16\pi^3 \epsilon_0 c^3} \int d\mathbf{k}_p \int_{\mathcal{D}_s} d\mathbf{k}_s \int_{\mathcal{D}_i} d\mathbf{k}_i \times \left[\frac{\omega_p(\omega_s+\omega_i)\eta_p^+}{n_p^+ n_p \eta_p}\right]^{1/2} \left[\frac{\omega_s \omega_i}{n_s n_i \eta_s \eta_i}\right] \times \frac{\psi_p(\mathbf{k}_p^+)}{\cos\theta_p^{\rm o}} s\left(\Delta k_z^d\right) s^*\left(\Delta k_z^u\right) e^{i\Phi_p} \delta(\omega_p - \omega_s - \omega_i) \times \delta\left(\Delta k_x^u\right)\delta\left(\Delta k_y^u\right)\hat{a}^\dagger(\mathbf{k}_p)\right\}|{\rm vac}\rangle. \quad (9)$$

We now transform the idler differential of Eq. (9) as $d\mathbf{k}_i = d\omega_i d\theta_i d\phi_i k_i^2 \eta_i \sin\theta_i$, which allows us to perform the ω_i integration trivially with the frequency δ function, setting $\omega_i = \omega_p - \omega_s$. The (θ_i, ϕ_i) integrations may then be performed using the identity that, for an arbitrary function $f(\theta_i, \phi_i)$,

$$\iint_{\Omega_i} d\theta_i d\phi_i \sin\theta_i f(\theta_i, \phi_i)\delta\left(\Delta k_x^u\right)\delta\left(\Delta k_y^u\right) = \frac{f\left(\theta_i^{\rm o}, \phi_i^{\rm o}\right)}{k_i^2 \cos\theta_i^{\rm o}} D_i\left(\theta_i^{\rm o}, \phi_i^{\rm o}\right), \quad (10)$$

where Ω_i is the solid angle implicit in $\mathcal{D}_i$. Here $D_i(\theta_i^{\rm o}, \phi_i^{\rm o})$ is a discrimination function that is unity if $(\theta_i^{\rm o}, \phi_i^{\rm o}) \in \Omega_i$ and zero otherwise. The angles $(\theta_i^{\rm o}, \phi_i^{\rm o})$ are those that zero the δ-function arguments in Eq. (10); it is thus readily shown that they follow from

$$\tan\phi_i^{\rm o} = \frac{k_p \sin\theta_p \sin\phi_p - k_s \sin\theta_s \sin\phi_s}{k_p \sin\theta_p \cos\phi_p - k_s \sin\theta_s \cos\phi_s}, \quad (11)$$

$$\sin\theta_i^{\rm o} = \frac{k_p \sin\theta_p \cos\phi_p - k_s \sin\theta_s \cos\phi_s}{k_i \cos\phi_i^{\rm o}}. \quad (12)$$

After integrating Eq. (9) over θ_i and ϕ_i in this way, the recombined pair state takes the form

$$|\psi_u\rangle = \left[\hat{I} - \sqrt{N_p}\int d\mathbf{k}_p \mathcal{E}(\mathbf{k}_p)\psi_p(\mathbf{k}_p) e^{i\Phi_p}\hat{a}^\dagger(\mathbf{k}_p)\right]|{\rm vac}\rangle, \quad (13)$$

with $\mathcal{E}(\mathbf{k}_p)$ given by

$$\mathcal{E}(\mathbf{k}_p) = \beta c^2 \frac{\hbar\omega_p}{n_p \cos\theta_p} \times \int_{\mathcal{D}_s} d\mathbf{k}_s \left[\frac{\omega_s\omega_i}{n_s n_i \eta_s}\right] \frac{D_i\left(\theta_i^{\rm o}, \phi_i^{\rm o}\right)}{\cos\theta_i^{\rm o}} |s(\Delta k_z)|^2, \quad (14)$$

with $\beta = \frac{d_{\rm eff}^2 L^2}{16\pi^3\epsilon_0 c^5}$ and where Eqs. (4), (5), (11), and (12) have been used to establish that $\mathbf{k}_p^+ = \mathbf{k}_p$ and thus $\Delta\mathbf{k}^u = \Delta\mathbf{k}^d \equiv \Delta\mathbf{k}$. We also determine the up-converted photon rate, which follows directly from

$$R_{\rm up} = \frac{1}{\Delta t}\int d\mathbf{k}_p \langle\psi_u|\hat{a}^\dagger(\mathbf{k}_p)\hat{a}(\mathbf{k}_p)|\psi_u\rangle = F_p \int d\mathbf{k}_p |\mathcal{E}(\mathbf{k}_p)\psi_p(\mathbf{k}_p)e^{i\Phi_p}|^2, \quad (15)$$

where $F_p = N_p/\Delta t$ is the pump photon rate.

There is clear similarity between the up-converted state of Eq. (13) and the attenuated pump of Eq. (A6). Comparison with the attenuated pump state is appropriate since, in the interference experiments of Sec. III C, the pump is attenuated until it has amplitude similar to the up-converted light. Both states represent the vacuum superposed with a weak single-photon state, with the latter term containing $\psi_p(\mathbf{k}_p)e^{i\Phi_p}$. In Eq. (A6) the single-photon term has been attenuated by a factor γ, while in Eq. (13) it contains $\mathcal{E}(\mathbf{k}_p)$ and carries a relative phase of π. To determine the degree of amplitude-amplitude coherence between these two states, we define the operator $\hat{u}^\dagger$ as the second term in square brackets in Eq. (13) and define $\hat{p}^\dagger$ in the same way for Eq. (A6). We consider the product state $|\psi_{p\otimes u}\rangle \equiv |\{\psi_p\}\rangle_p|\psi_u\rangle_u$, where ket subscripts denote the relevant Hilbert subspaces. It then follows that

$$|\psi_{p\otimes u}\rangle = (\hat{I} + \hat{p}^\dagger + \hat{u}^\dagger)|{\rm vac}\rangle_p|{\rm vac}\rangle_u, \quad (16)$$

where a small term corresponding to one photon in each mode has been dropped. The equal-time mutual coherence function of the attenuated pump and up-converted states may then be found from the usual methods [26] as

$$G_{pu}^{(1)}(\mathbf{k}_p, \mathbf{k}_u) = \langle\psi_{p\otimes u}|\hat{a}^\dagger(\mathbf{k}_p)\hat{a}(\mathbf{k}_u)|\psi_{p\otimes u}\rangle = N_p e^{i\pi}\gamma^*\mathcal{E}(\mathbf{k}_u)\psi_p^*(\mathbf{k}_p)\psi_p(\mathbf{k}_u). \quad (17)$$

The normalized degree of mutual coherence follows as

$$g_{pu}^{(1)}(\mathbf{k}_p, \mathbf{k}_u) = \frac{G_{pu}^{(1)}(\mathbf{k}_p, \mathbf{k}_u)}{\left\{G_{pp}^{(1)}(\mathbf{k}_p, \mathbf{k}_p)G_{uu}^{(1)}(\mathbf{k}_u, \mathbf{k}_u)\right\}^{1/2}}, \quad (18)$$

where $G_{\epsilon\epsilon}^{(1)}(\mathbf{k}_\epsilon, \mathbf{k}_\epsilon)$ is the self-coherence function of mode ϵ. Since the weighting functions of the two single-photon states are the only factors appearing in Eq. (17), $g_{pu}^{(1)}(\mathbf{k}_p, \mathbf{k}_u)$ is directly shown to have unit modulus, implying perfect mutual amplitude coherence.

Our analysis here neglects the effects of losses on the SPDC, which are experimentally inevitable; however, it has been established that the two-photon part of the down-converted state retains a pure state description even when losses are introduced into the Hamiltonian [37,38]. With the up-converted state consequently being the pure state of Eq. (13), and with Eq. (A6) similarly representing the attenuated pump, it is thus expected that interfering the pump and up-converted light will produce temporally stable fringes. This will be experimentally demonstrated in Sec. III C and lies in clear contrast to experiments performed with independent sources, which interfere for observation times less than the reciprocal of the bandwidth and require a density-matrix formulation for their description [39].

There are further implications of our results. For example, it may similarly be shown that $g_{uu}^{(1)}(\mathbf{k}_u, \mathbf{k}_u')$ has unit modulus, so $|\psi_u\rangle$ has perfect spatial coherence. In addition, consider the dimensionless quantity $\mathcal{E}(\mathbf{k}_p)$ of Eq. (14); it has no dependence on the pump amplitude and instead expresses only the effects of the photon pair generation and recombination process. In Eq. (13) it multiplies the input amplitude $\psi_p(\mathbf{k}_p)e^{i\Phi_p}$ to produce the up-converted amplitude; it is then simply a linear coherent transfer function that describes all effects of the down-conversion–up-conversion process. It is

perhaps surprising that the basic result of Eqs. (13) and (14) could take on such a simple form.

While the preceding results are general, we now make some simplifying assumptions. As in the experiment here, consider the case of a narrow-band pump, with the spatial dependence of the up-converted amplitude being of interest. We transform the second integral of Eq. (15) from $\mathbf{k}_p$ to the variables $(\omega_p, \theta_p, \phi_p)$ and let (see the Appendix) $\psi_p(\mathbf{k}_p) = \frac{\mathcal{A}(\omega_p)}{\sqrt{\eta_p k_p}}\mathcal{F}(\theta_p, \phi_p|\omega_p)$, with $\mathcal{A}(\omega_p)$ being the pump spectrum and $\mathcal{F}(\theta_p, \phi_p|\omega_p)$ the angular spectrum at a given ω_p. Then, we take the narrow-band limit $|\mathcal{A}(\omega_p)|^2 \to \delta(\omega_p - \omega_p^{\circ})$ and perform the ω_p integration, with the result that

$$R_{\rm up} = F_p \iint d\theta_p d\phi_p \sin\theta_p \left|\mathcal{E}_{\omega_p^{\circ}}(\theta_p, \phi_p)\mathcal{F}\left(\theta_p, \phi_p|\omega_p^{\circ}\right)e^{i\Phi_p}\right|^2, \tag{19}$$

where, now with $\omega_i = \omega_p^{\circ} - \omega_s$,

$$\mathcal{E}_{\omega_p^{\circ}}(\theta_p, \phi_p) = \beta\frac{\hbar\omega_p^{\circ}}{n_p\cos\theta_p}\int d\omega_s \frac{n_s\omega_s^3\omega_i}{n_i} \times \iint_{\Omega_s} d\theta_s d\phi_s \frac{\sin\theta_s}{\cos\theta_i^{\circ}} D_i\left(\theta_i^{\circ}, \phi_i^{\circ}\right)|s(\Delta k_z)|^2. \tag{20}$$

From the form of Eq. (19) and through its comparison with Eq. (A5), we identify $\mathcal{E}_{\omega_p^{\circ}}(\theta_p, \phi_p)$ as the amplitude transfer function for a single-frequency pump. It is thus relevant to the experiments performed here and may be regarded as a simplification of $\mathcal{E}(\mathbf{k}_p)$ of Eq. (14).

Finally, we consider the further limit of a pump beam waist that is quite wide in the crystal. This limit is properly taken in Eq. (19) as $|\mathcal{F}(\theta_p, \phi_p|\omega_p^{\circ})|^2 \to k_p^2\delta(k_p\sin\theta_p\cos\phi_p)\delta(k_p\sin\theta_p\sin\phi_p)$, with the result that $R_{\rm up} = F_p|\mathcal{E}_{\omega_p^{\circ}}^{\rm WP}e^{i\Phi_p}|^2$, where

$$\mathcal{E}_{\omega_p^{\circ}}^{\rm WP} = \beta\frac{\hbar\omega_p^{\circ}}{n_p}\int d\omega_s \frac{n_s\omega_s^3\omega_i}{n_i} \times \iint_{\Omega_s} d\theta_s d\phi_s \frac{\sin\theta_s}{\cos\theta_i^{\circ}} D_i\left(\theta_i^{\circ}, \phi_i^{\circ}\right)|s(\Delta k_z)|^2. \tag{21}$$

We term $\mathcal{E}_{\omega_p^{\circ}}^{\rm WP}$ the amplitude transfer efficiency. In Eq. (21), $(\theta_i^{\circ}, \phi_i^{\circ})$ are now to be evaluated at $\theta_p = 0$, which follow from Eqs. (11) and (12) as $(\theta_i^{\circ}, \phi_i^{\circ}) = (\arcsin[\frac{n_s\omega_s}{n_i\omega_i}\sin\theta_s], \phi_s - \pi)$. Also, it is clear that $\mathcal{E}_{\omega_p^{\circ}}^{\rm WP} = \mathcal{E}_{\omega_p^{\circ}}(\theta_p, \phi_p)|_{\theta_p=0}$.

B. Evaluations

We now evaluate the theoretical results for an idealized experimental up-conversion system. For clarity, we denote angles in free space with tildes; e.g., $\tilde{\theta}_p$ is related to θ_p by Snell's law. After exiting the first crystal, we assume that the SPDC is limited by a circular aperture to a cone of angular radius $\tilde{\theta}_c$, which specifies the integration domains of $\mathbf{k}_s$ and $\mathbf{k}_i$ in Eq. (1). Thus Eq. (20) becomes

$$\mathcal{E}_{\omega_p^{\circ}}(\theta_p, \phi_p) = \beta\frac{\hbar\omega_p^{\circ}}{n_p\cos\theta_p}\int d\omega_s S(\omega_s), \tag{22}$$

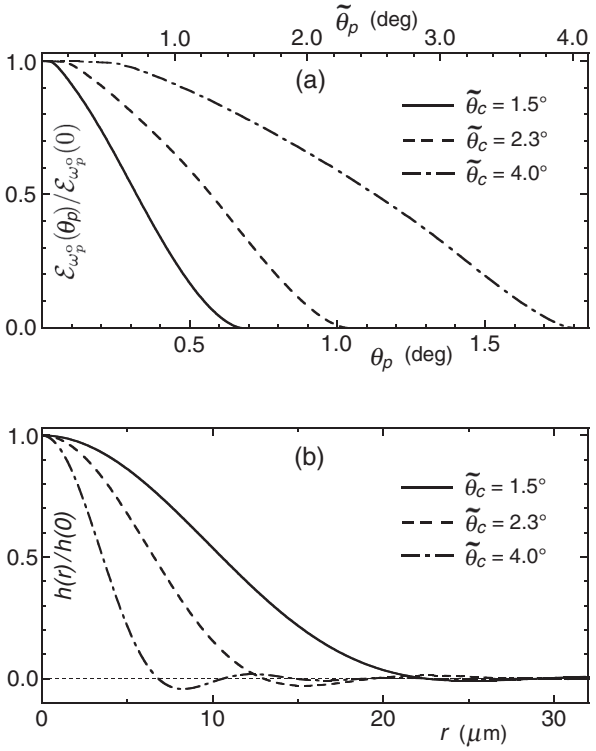

FIG. 1. (a) Scaled to unit height, transfer functions $\mathcal{E}_{\omega_p^{\circ}}(\theta_p)$ for aperture radius $\tilde{\theta}_c = 1.5^{\circ}$ ($\Delta T = 1\,^{\circ}$C), 2.3° ($\Delta T = 1.5\,^{\circ}$C), and 4.0° ($\Delta T = 2\,^{\circ}$C), with $\tilde{\theta}_p = \arcsin(n_p\sin\theta_p)$. (b) Amplitude point spread functions $h(r)$ for the cases from (a), also scaled to unit height; the actual heights $h(0)$ are 1.8×10^{-11} μm^{-1} ($\tilde{\theta}_c = 1.5^{\circ}$), 8.8×10^{-11} μm^{-1} ($\tilde{\theta}_c = 2.3^{\circ}$), and 5.7×10^{-10} μm^{-1} ($\tilde{\theta}_c = 4.0^{\circ}$).

where

$$S(\omega_s) = \frac{n_s\omega_s^3\omega_i}{n_i}\int_0^{\Theta_s} d\theta_s \int_0^{2\pi} d\phi_s \frac{\sin\theta_s}{\cos\theta_i^{\circ}} \times D_i\left(\theta_i^{\circ}, \phi_i^{\circ}\right)|s(\Delta k_z)|^2, \tag{23}$$

with $\Theta_s = \arcsin[\sin\tilde{\theta}_c/n_s]$ the angular limit within the crystal. Here $D_i(\theta_i^{\circ}, \phi_i^{\circ})$ represents the circular limiting aperture in idler variables. In particular, $D_i(\theta_i^{\circ}, \phi_i^{\circ})$ is zero if $\theta_i^{\circ} > \Theta_i \equiv \arcsin[\sin\tilde{\theta}_c/n_i]$, while it has rotational invariance in ϕ_i°. It is also notable that the pump angles (θ_p, ϕ_p) are not seen in $S(\omega_s)$ in Eq. (23); instead, they enter implicitly through $(\theta_i^{\circ}, \phi_i^{\circ})$ from Eqs. (11) and (12).

We have integrated Eqs. (22) and (23) numerically for parameters as in the experiments to be presented here. For a circular aperture the results are independent of ϕ_p, so we take the transfer function as simply $\mathcal{E}_{\omega_p^{\circ}}(\theta_p)$. The pump wavelength is considered to be 532 nm. The nonlinear crystals are assumed to be MgO-doped, periodically poled lithium niobate of length $L = 5$ mm with $d_{\rm eff} = 2d_{33}/\pi$ [33], and we take $d_{\rm eff}$ as 1.5×10^{-11} m/V. The extraordinary refractive index used here follows from a Sellmeier equation [40], while its temperature dependence is a quadratic fit to data that have been reported elsewhere [41]. To be close to the experimental situation, we assume that $\Delta\mathbf{k} = 0$ for axial degenerate SPDC at crystal temperature $T_{\circ} = 50\,^{\circ}$C and calculate the poling wave vector $\mathbf{k}_g$ that satisfies this condition.

Figure 1(a) shows $\mathcal{E}_{\omega_p^o}(\theta_p)$ for several aperture radii $\tilde{\theta}_c$. The curves there are scaled to unit height; actual heights are 3.5×10^{-8} for $\tilde{\theta}_c = 1.5^\circ$ to 5.9×10^{-8} for $\tilde{\theta}_c = 2.3^\circ$ and 1.1×10^{-7} for $\tilde{\theta}_c = 4.0^\circ$. It can be seen that all curves monotonically decrease in θ_p and reach zero when the external pump angle $\tilde{\theta}_p$ is essentially $\tilde{\theta}_c$. This cutoff angle may be understood as follows. As the angle of a plane-wave pump in the crystal is increased, the SPDC cone increases similarly in angle. Up-conversion requires intact photon pairs, which fall on opposing points with respect to the SPDC cone center; thus intact pairs no longer pass through the aperture when the *center* of the SPDC cone reaches the edge of the limiting aperture. This condition occurs for $\tilde{\theta}_p = \tilde{\theta}_c$ and up-conversion ceases. Additionally, it should be noted that crystal temperatures in Fig. 1(a) are slightly dropped to $T_\circ - \Delta T$ (see caption), as is done in our experiments, since it increases the detected signal by slightly opening the SPDC cone.

The transfer function $\mathcal{E}_{\omega_p^o}(\theta_p)$ may be considered an angular amplitude spectrum; it follows that its corresponding transverse spatial distribution in the up-conversion crystal may be found from its two-dimensional inverse Fourier transform (see Ref. [42], Sec. 3.10.1). With $\mathcal{E}_{\omega_p^o}(\theta_p)$ being ϕ_p invariant, the inverse transform simplifies to the Fourier-Bessel integral (see Ref. [42], Sec. 2.1.5) which, in unitary form, may be written here as

$$h(r) = \frac{1}{k_p} \int_0^\infty dk_\perp k_\perp \mathcal{E}_{\omega_p^o}(k_\perp/k_p) J_0(k_\perp r), \tag{24}$$

where $k_\perp = k_p \theta_p$ in a paraxial approximation and r is the radial coordinate in the waist plane. It is notable that $h(r)$ represents the point spread function of the up-conversion system; i.e., multiplying the pump angular spectrum $\mathcal{F}(\theta_p, \phi_p|\omega_p^o)$ by the transfer function $\mathcal{E}_{\omega_p^o}(\theta_p)$ is equivalent to convolving the original transverse pump amplitude with $h(r)$ in the waist plane in the up-conversion crystal (see Ref. [42], Sec. 2.3.2). Figure 1(b) shows $h(r)$ for the same three cases of Fig. 1(a), with Eq. (24) being integrated numerically. The case for $\tilde{\theta}_c = 1.5^\circ$ exhibits a Gaussian-like distribution of width (e^{-1} radius) 12.5 μm, with faint secondary rings. The case for $\tilde{\theta}_c = 4.0^\circ$ presents a distribution of width only 4.2 μm, with secondary rings having higher contrast, while the case for $\tilde{\theta}_c = 2.3^\circ$ (width 7.7 μm) shows intermediate behavior.

We now consider a more realistic optical system. Our assumption that the SPDC state of the first crystal is simply copied in the second is often inadequate, and we consider the effect of imperfect temporal dispersion compensation. In particular, we assume that the amplitude $\psi(\mathbf{k}_s, \mathbf{k}_i)$ from the first crystal is now cast into the second as $\psi(\mathbf{k}_s, \mathbf{k}_i) e^{i[\varphi_s(\omega_s)+\varphi_i(\omega_i)]}$, where $\varphi_\epsilon(\omega_\epsilon)$ represents the phase accumulated along the signal ($\epsilon = s$) or idler ($\epsilon = i$) optical path. This phase factor then appears throughout the analysis that follows in Sec. II A and ultimately falls within the integral of Eq. (22) as a factor multiplying $S(\omega_s)$. Then, transforming the integration variable from ω_s to $\Delta\omega = \omega_s - \omega_d$, with $\omega_d = \omega_p^o/2$, Eq. (22) may be written as

$$\mathcal{E}_{\omega_p^o}(\theta_p) = \beta' \int d\Delta\omega\, S(\omega_d + \Delta\omega) e^{i[\varphi_s(\omega_d+\Delta\omega)+\varphi_i(\omega_d-\Delta\omega)]}, \tag{25}$$

where β' is the coefficient of the integral of Eq. (22).

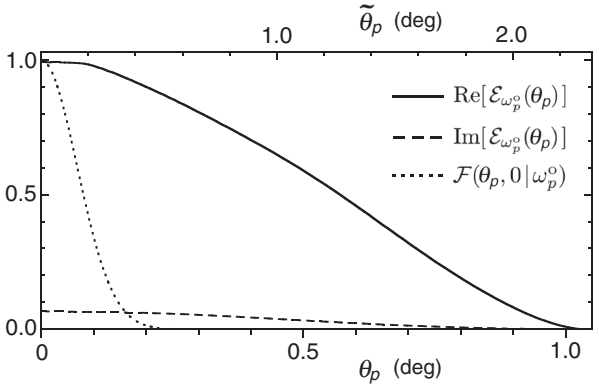

FIG. 2. Transfer function $\mathcal{E}_{\omega_p^o}(\theta_p)$ for aperture radius $\tilde{\theta}_c = 2.3^\circ$ and temporal dispersion parameters as in the experiments performed here, normalized to unit height for the analogous dispersion-free case [see Fig. 1(a)]. Shown for comparison is the Gaussian pump angular spectrum $\mathcal{F}(\theta_p, 0|\omega_p^o)$ used in our experiments, normalized to unit height.

In our experiments here, the signal and idler photons travel along a single path, so $\varphi_s(\omega)$ and $\varphi_i(\omega)$ are the same function $\varphi(\omega)$. We take $\varphi(\omega)$ as the phase of an axial path from the center of the down-conversion crystal, through the optical system, to the center of the second crystal. Expanding the argument of the exponential in Eq. (25) in powers of $\Delta\omega$, only even-order terms survive, with the result

$$\varphi(\omega_d + \Delta\omega) + \varphi(\omega_d - \Delta\omega) = \sum_{n=2,4,6,\ldots} \frac{2\varphi^{(n)}\Delta\omega^n}{n!}, \tag{26}$$

where $\varphi^{(n)}$ denotes $\frac{\partial^n \varphi(\omega)}{\partial \omega^n}|_{\omega_d}$ and the zeroth-order term has been dropped to neglect the absolute phase. The term $\varphi^{(2)}$ is the modal group delay dispersion, with others denoting dispersion of higher order. For the experimental system described in Sec. III A, we determine $\varphi(\omega)$ from the system geometry and then calculate that $\varphi^{(2)} = 33.0$ fs^2 and $\varphi^{(4)} = -2.54 \times 10^4$ fs^4; higher-order terms are not significant over the integration bandwidth.

Inserting Eq. (26) into Eq. (25), we perform the integration numerically and obtain the result shown in Fig. 2. It can be seen that $\mathcal{E}_{\omega_p^o}(\theta_p)$ is now complex, with a small imaginary part. It is notable that *temporal* dispersion thus manifests itself here as a *spatial* phase in the up-converted state. Taking the Fourier-Bessel transform of $\mathcal{E}_{\omega_p^o}(\theta_p)$, we similarly find that $h(r)$ has a small imaginary part, although the width and modulus of $h(r)$ are within 1% of the analogous dispersion-free case from Fig. 1(b); thus we do not show this result here. Also shown in Fig. 2 is the amplitude angular spectrum $\mathcal{F}(\theta_p, 0|\omega_p^o)$ of the circular Gaussian pump beam used in our experiments; it is so narrow that $\mathcal{E}_{\omega_p^o}(\theta_p)$ will have little effect on its shape. The value of $\varphi^{(2)}$ can be readily adjusted in the experiments and it here provides a good balancing of the quartic dispersion due to $\varphi^{(4)}$; indeed, $|\mathcal{E}_{\omega_p^o}(0)|$ is 0.995 of the unchirped case shown in Fig. 1(a). However, we emphasize that stronger dispersive effects rapidly lead to significantly more attenuation and changes in the shape of $\mathcal{E}_{\omega_p^o}(\theta_p)$, although we do not present such results here.

Finally, we point out that our approach may be applied to a different class of up-conversion experiments and we provide a direct comparison with previous experimental data. In particular, it is possible to introduce a relative time delay between the signal and idler photons and to then observe the up-conversion rate as a function of the delay [18]. This provides a measure of the synchronization of the pairs at a femtosecond level, allowing ultrahigh-resolution observations of effects such as Franson dispersion cancellation [19]. To introduce such a time delay in our results, we now consider the quantum state in the first crystal to be transformed to that in the second crystal as

$$\psi(\mathbf{k}_s, \mathbf{k}_i) \rightarrow \psi(\mathbf{k}_s, \mathbf{k}_i) e^{i\omega_s \tau} e^{i[\varphi_s(\omega_s)+\varphi_i(\omega_i)]}, \tag{27}$$

where τ is the relative delay of the signal mode and we have also included the residual chirp phase terms discussed previously. The exponentials in the expression (27) again carry through the analysis, to finally appear as factors multiplying $S(\omega_s)$ in the integrand of Eq. (22), as in the previous case.

We again assume a circular limiting aperture but now, for simplicity, take the wide-pump limit discussed earlier. The amplitude transfer efficiency $\mathcal{E}^{\mathrm{WP}}_{\omega_p^o} = \mathcal{E}_{\omega_p^o}(\theta_p, \phi_p)|_{\theta_p=0}$ follows from Eq. (22) with the phase terms introduced as

$$\mathcal{E}_o(\tau) = \beta' \int_0^\infty d\omega_s S(\omega_s) e^{i\omega_s \tau} e^{i[\varphi_s(\omega_s)+\varphi_i(\omega_i)]}, \tag{28}$$

where we have renamed this quantity as $\mathcal{E}_o(\tau)$ and it is understood that $S(\omega_s)$ is to be evaluated with $\theta_p = 0$ in Eq. (23). Thus $\mathcal{E}_o(\tau)$ can be nearly the Fourier transform of $S(\omega_s)$, depending on the significance of the chirp phase terms.

To evaluate $\mathcal{E}_o(\tau)$, we use the experimental parameters of Ref. [19], some of which (the type of nonlinear crystals, their temperature, pump wavelength, $\tilde{\theta}_c = 2.3^\circ$) are identical to parameters assumed earlier here. In Ref. [19], however, the signal and idler photons propagate along separate paths before their recombination. Thus the analog of Eq. (26) now takes the form

$$\varphi_s(\omega_d + \Delta\omega) + \varphi_i(\omega_d - \Delta\omega) = \sum_{n=2}^{\infty} \frac{\gamma_n \Delta\omega^n}{n!}, \tag{29}$$

where $\gamma_n = [\varphi_s^{(n)} + (-1)^n \varphi_i^{(n)}]$. These two distinct paths were obtained by sending the two halves of the SPDC emission cone into different directions, which differs from the assumptions of our theoretical development. However, in the wide-pump limit, it may be shown that our theory produces fully correct results for this experimental situation, although we do not prove this point here.

We have ray traced the optical system of Ref. [19] to calculate the path phases and, for the configuration used to obtain the data of their Fig. 3(d), we find $\gamma_2 = 46.0$ fs^2, $\gamma_3 = -3.52 \times 10^3$ fs^3, and $\gamma_4 = -4.07 \times 10^4$ fs^4. We compare our calculation of the normalized rate $\mathcal{R}(\tau) \equiv |\mathcal{E}_o(\tau)|^2$ with the original experimental data in our Fig. 3. In both plots, the main peak has been centered at $\tau = 0$ for comparison. In the theory, this shift (5.6 fs) is necessary because of cubic dispersion; in particular, γ_3 is responsible for moving the peak of $|\mathcal{E}_o(\tau)|$ of Eq. (28) to $\tau = 5.6$ fs. It can be seen that the general agreement is quite good in Fig. 3, with both results showing a narrow central peak, accompanied by right-skewed secondary maxima which, in the calculation, is also a consequence of γ_3. The temporal widths of features are close, although the experimental result is slightly wider. For example, the theoretical full width at half maximum is 22.1 fs, as compared to the experimental width of 24.7 fs. Such differences could arise if the experimental spectrum $S(\omega_s)$ were slightly narrower in the near-Fourier relation of Eq. (28); this could occur from crystal or optical component bandwidth limitations.

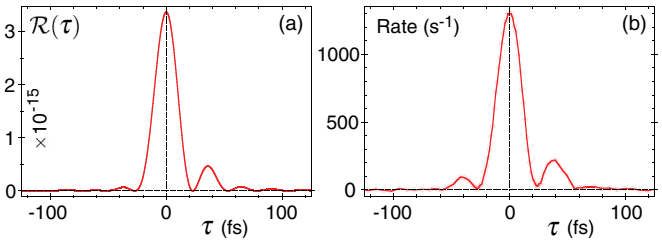

FIG. 3. (a) Up-conversion rate efficiency $\mathcal{R}(\tau)$ evaluated for dispersion parameters consistent with the up-conversion rate data of Fig. 3(d) of Ref. [19], compared to the original data reproduced in (b).

We add that our results are normalized in the sense that $F_p \mathcal{R}(\tau)$ is the predicted recombination rate. For the pump power in Ref. [19] (1 W incident on the SPDC crystal), this predicts a rate of 9.0×10^3 s^{-1} at the peak of $\mathcal{R}(\tau)$ in Fig. 3(a). The experimental result reaches 14% of this rate; however, this experiment has losses from crystal Fresnel reflections, poling imperfections, filter transmissions, fiber coupling, and detector quantum efficiency. Such losses were not specified in Ref. [19], but could quite possibly account for this difference in scale. In any case, the general agreement of the two results of Fig. 3 indicates that our theoretical approach may be readily extended to include effects of temporal delays, producing information on the ultrafast properties of photon pairs.

To summarize, the theoretical approach developed here is quite general. In addition to the effects of our particular interest, it could be applied to study the dependence of the recombination rate on parameters such as pump wavelength and bandwidth, crystal temperature, and phase aberrations of the optical relay system. More fundamentally, it may be used to draw conclusions about the phase and temporal properties of the two-photon amplitude itself, providing information well beyond the capabilities of common techniques such as direct pair detection.

III. EXPERIMENTS

A. Methods

Our experimental goals were to observe the up-converted modal structure and to investigate its mutual coherence with the pump. We employed a pump beam that, in the far field, was much narrower than $\mathcal{E}_{\omega_p^o}(\theta_p)$ (see Fig. 2 for the Gaussian pump mode employed); thus the pump beam should be well reconstructed. Far more significant effects arise from the coupling of the up-converted amplitude to the single-mode optical fiber used for detection. Thus our analysis here will

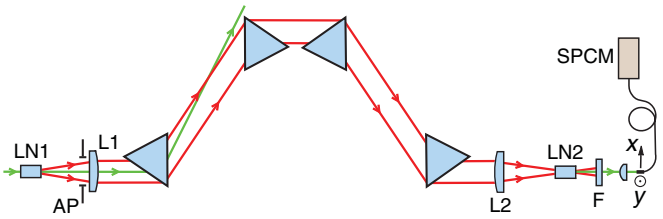

FIG. 4. Experimental diagram (not to scale). A pump beam of wavelength 532 nm produces SPDC in lithium niobate crystal LN1. The SPDC passes through a limiting aperture AP, is collimated by lens L1, travels through a four-prism compressor, and is focused by lens L2 into a second crystal LN2. The SPDC exiting LN2 is removed with a filter F and the up-converted light is coupled into a detector (SPCM) via a single-mode fiber, whose tip may be scanned in the xy plane.

account for fiber effects and only later will we consider the small effects of $\mathcal{E}_{\omega_p^\circ}(\theta_p)$.

Another comment to be made is that, under our experimental conditions, entangled photon pair recombination appears to be the only significant contribution to the detected signal and the up-conversion rate between members of different pairs is negligible. This may be noted from experiments conducted under quite similar conditions [19], in which large temporal desynchronization of pair members reduced the detected signal to negligible levels above the dark count; otherwise it would fall to a level determined by the rate of random up-conversion events. Thus such events do not contribute significantly to the detected signal in the experiments performed here.

The pump laser was continuous wave with wavelength 532 nm and single-mode linewidth 5 MHz and had a circular Gaussian spatial mode. The nonlinear crystals employed were periodically poled, MgO-doped lithium niobate of length 5 mm. Both had a poling period that produced $\Delta\mathbf{k} = 0$ for axial, degenerate-frequency photon pairs at approximately 50 °C. They were kept in ovens at 1.5 °C below this temperature which slightly opens the SPDC cone, as has been noted with other poled crystals [43]; this optimizes the signal levels in our experiment.

Figure 4 shows our experimental geometry that was, in many respects, similar to that used in studies of other aspects of photon pair recombination [16–20]. The pump beam was focused to a waist with $w_\circ = 45$ μm at the center of the first crystal. The light emerging from the crystal passed through a circular aperture of radius $\tilde{\theta}_c = 2.3^\circ$ and was collimated by a lens of 75 mm focal length. This light then encountered a temporal compression system having four identical prisms of SF10 glass with 60° apex angles. The tip-to-tip distance between either the first or the second pair of prisms was 538 mm. The prism rotational angles were set for minimum deviation at degenerate wavelength 1064 nm and the SPDC followed the prism path, while the pump light was deflected out of the system by the first prism. The polarization directions of the pump beam and the down-conversion were all in the plane of Fig. 4.

After the prisms, the SPDC encountered another lens, again of focal length 75 mm, and was focused at the center of the second crystal. The light then passed through a green filter that removed the remaining SPDC but transmitted the up-converted light. The crystal center was imaged by an aspherical lens with a demagnification of 1/25; thus the imaged mode was expected to have a waist with $w'_\circ = \frac{1}{25} w_\circ = 1.80$ μm. In this plane was placed the tip of a single-mode optical fiber (Nufern 460HP), whose other end was connected to a SPCM-AQR-13-FC photon counting module. Initially, the prism insertions were set so as to null the group delay dispersion calculated for the path connecting the centers of the two crystals. Then the detected up-converted photon rate was maximized by optimizing the dispersion using the third prism of Fig. 4, which required further insertion adjustment of less than 1 mm. This compression setting was used throughout all work here.

The fiber tip was mounted on a piezoelectric stage that allowed it to be scanned in the plane transverse to the propagation direction, taken here as the xy plane. Monitoring the detection rate as a function of fiber position thus allowed investigation of the up-converted spatial mode shape. If the up-converted amplitude is $A_u(x, y)$ and the fiber mode is represented by $A_f(x, y)$ with the fiber centered in the xy plane, the detected signal depends on the modal overlap [44]

$$\mathcal{H}(x, y) = \iint_{-\infty}^{\infty} A_u(x', y') A_f^*(x' - x, y' - y) dx' dy', \quad (30)$$

where (x, y) represent the off-axis displacement of the fiber and A_u and A_f are each normalized to unit power. In particular, the photon detection rate is proportional to $\eta(x, y) \equiv |\mathcal{H}(x, y)|^2$. The modal amplitude A_f will be taken as a Gaussian function of e^{-1} radius $w_f = 1.75$ μm, based on the fiber specifications.

Finally, to obtain pump modes in addition to the laser's Gaussian mode, mode converters could be introduced between the laser output and the first lens of Fig. 4. Such mode converters transform the spatial mode but leave $w_\circ$ unchanged. To produce a Hermite-Gaussian HG_{10} mode, the Gaussian laser beam entered a phase-locked Mach-Zehnder interferometer mode converter [45]. Here the interferometer port that was utilized contained two oppositely phased Gaussian laser modes, whose centers were separated by approximately $1.1 w_\circ$; such a beam may be calculated as having an inner product greater than 0.99 with an ideal HG_{10} mode. To produce a Laguerre-Gaussian LG_{01} mode, the Mach-Zehnder output was in turn transformed with a cylindrical lens mode converter [46]. These are standard techniques that will not be discussed further here. The power incident on the crystal was maintained at 1 W in all cases, with the laser power setting being used to compensate losses in the mode converters.

B. Modal results

During a scan, the fiber tip was placed at each sample point in the xy plane for 1 s while the detector signal was measured. The background level was determined by averaging the data from the scan perimeter, since the desired signal there appeared negligible; this background (approximately 225 s^{-1}, a few counts above intrinsic detector dark count) was subtracted from modal data shown here. Then the data were least-squares curve fit to $\eta(x, y)$, with $A_u(x, y)$ assumed

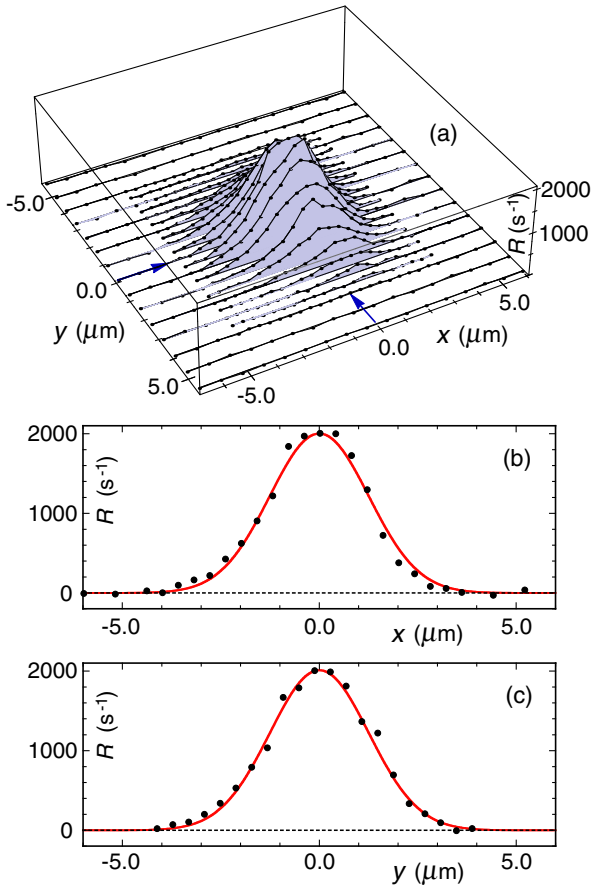

FIG. 5. (a) Two-dimensional scans of the detected up-conversion rate R as a function of transverse fiber position are shown for the case of a circular Gaussian pump beam. (b) and (c) Data for scan lines passing closest to the origin are shown as points, accompanied by the theoretical fit (solid lines). Arrows in (a) indicate the lines along which (b) and (c) are taken (at $y = -0.12$ μm and $x = 0.02$ μm, respectively).

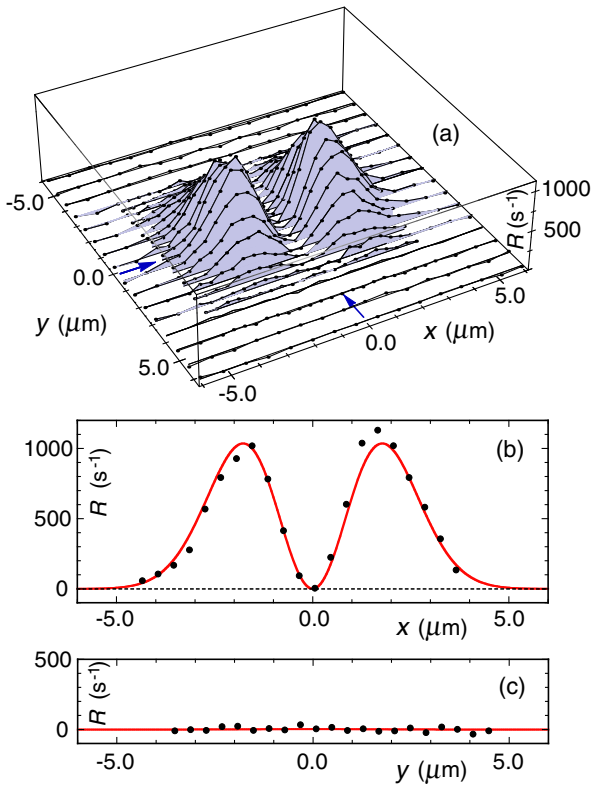

FIG. 6. (a) Experimental results for the detected up-conversion rate R as in Fig. 5, but for an HG_{10} pump beam. (b) and (c) Results for the scan lines passing closest to the origin (at $y = 0.08$ μm and $x = 0.06$ μm, respectively).

to have, for now, the functional form of the original pump mode function. The fitting parameters used were the height and width of $\eta(x, y)$ and the position of the center of the data. This position is then taken as the plot origin throughout the results shown here.

Figure 5 shows experimental results for the case of a Gaussian pump mode. The distribution presents a generally Gaussian shape with maximum height approximately 2×10^3 s^{-1}. It is notable that Eq. (30) is here the convolution of two Gaussians, so the predicted form of $\mathcal{H}(x, y)$ is then itself a Gaussian of e^{-1} radius $w_{\mathcal{H}} = (w_\circ'^2 + w_f^2)^{1/2}$. In turn, it follows that $\eta(x, y)$ is Gaussian with width parameter $w_\eta = w_{\mathcal{H}}/\sqrt{2}$, which is found directly from our fitting procedure as $w_\eta = 1.78$ μm. Figures 5(b) and 5(c) show the x and y scan lines of the data passing nearest the origin, which are there compared with the fit to $\eta(x, y)$. It can be seen that the agreement is excellent. Finally, the known value of w_f and the fitted value of w_η allow the implied beam width to be estimated as $w_\circ' = (2w_\eta^2 - w_f^2)^{1/2} = 1.81$ μm, which is quite close to that expected.

Analogous data for the case of an HG_{10} pump mode are shown in Fig. 6, where maximum signal levels are just above 1.1×10^3 s^{-1}. It can be seen that the result bears a strong resemblance to the pump intensity, exhibiting two similar lobes separated by a trough where the signal falls to negligible levels. The convolution of Eq. (30) can here again be performed in closed form, and one finds that $\mathcal{H}(x, y)$ has the same functional form as an HG_{10} pump mode amplitude but with width $w_{\mathcal{H}} = (w_\circ'^2 + w_f^2)^{1/2}$. From the curve fit of $\eta(x, y)$ to the data, we find that $w_\eta = 1.77$ μm, from which we can calculate an estimate of $w_\circ'$ as $w_\circ' = (2w_\eta^2 - w_f^2)^{1/2} = 1.79$ μm, which is once again similar to that expected. The plots of Figs. 6(b) and 6(c) show good agreement between the data and the theoretical fit to $\eta(x, y)$ for the scan lines passing nearest the origin. It is quite notable that the data of Fig. 6(c) show negligible levels in the trough between the lobes; this result is consistent with the form of Eq. (30) when the fiber is centered at a zero crossing of the up-converted mode.

Figure 7 shows data for the case of an LG_{01} pump mode, where the highest signal levels are approximately equal to 600 s^{-1}. The data here have some irregularity, in part due to the increased relative noise at the lower detection rates. However, it is still possible to see structure that bears significant resemblance to an LG_{01} intensity and, while the ring of maximum brightness is somewhat uneven, the central minimum is quite deep. This depth is more easily seen in Figs. 7(b) and 7(c), where the central data points are scarcely above zero. To provide theoretical comparisons with $\eta(x, y)$ here, the convolution of Eq. (30) must be performed numerically. From these results, we find that the resulting parameter $w_\circ' =$

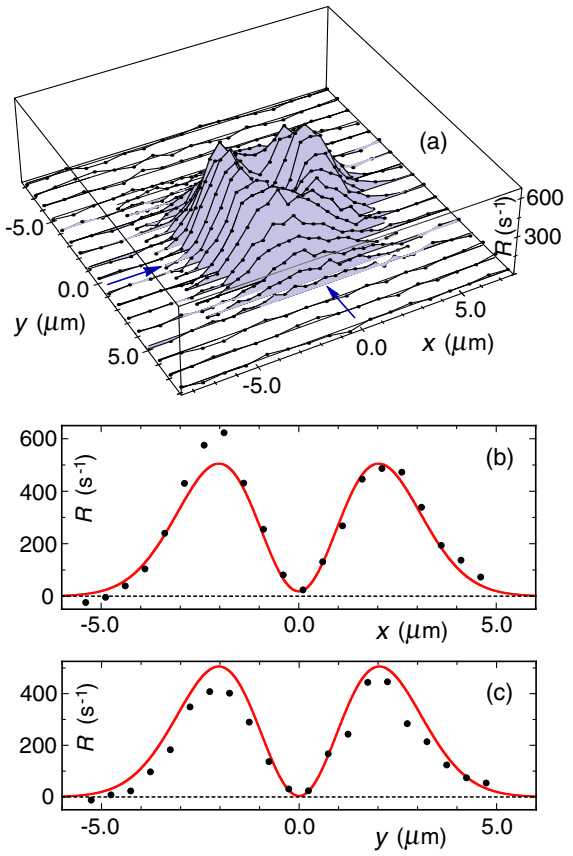

FIG. 7. (a) Experimental results for the detected up-conversion rate R as in Fig. 5, but for an LG_{01} pump beam. (b) and (c) Results for the scan lines passing closest to the origin (at $y = 0.24$ μm and $x = 0.11$ μm, respectively).

2.28 μm, which is slightly larger than expected. Still, the comparison of the theoretical curve with the data in Figs. 7(b) and 7(c) is generally good, so the modal shape is reasonably reproduced.

In summary, the agreement between the experimental results and calculations is good and we have demonstrated that the up-converted spatial intensity resembles that of the pump. It is also clear that the signal levels fall in the series of data from Figs. 5–7; such behavior is consistent with Eq. (30), which predicts that the coupled power decreases as the up-converted mode increasingly differs from the fiber mode. As for the effect of the point spread function of Sec. II B, we have computed its convolutional effects in some cases, but it is so narrow (7.7 μm e^{-1} width in the up-conversion plane) that it would increase measured widths by only approximately 1%. Thus it has little effect on our results even though, of course, it could produce significant effects under other experimental conditions.

C. Interference with pump

A second type of measurement was performed to investigate the coherence of the up-converted light and, to a limited extent, to observe the phase structure of the up-converted amplitude. The approach was straightforward, using a beam splitter of 0.95 reflectivity to mix the up-converted light and the pump light. The single-mode fiber of Fig. 4 was disconnected from the detector and its output was collimated and reflected from the beam splitter. The pump light was taken from that deflected by the first prism of Fig. 4, which was attenuated, beam expanded with two positive lenses, and then transmitted by the same beam splitter. Further, the beam expander had a small pinhole at its focus that, depending on the pump mode employed, passed either the center of Gaussian mode or the center of *one* of the two lobes of the HG_{10} mode. Considerable care was obviously necessary in the spatial mode matching of the two interfering beams and in balancing their amplitudes. Further, we stress that the interference occurs between *single spatial modes*, due to the single-mode fiber and the pinhole in the two interfering sources. Finally, the mixed beams were focused to couple into a multimode fiber, whose other end was now connected to the detector.

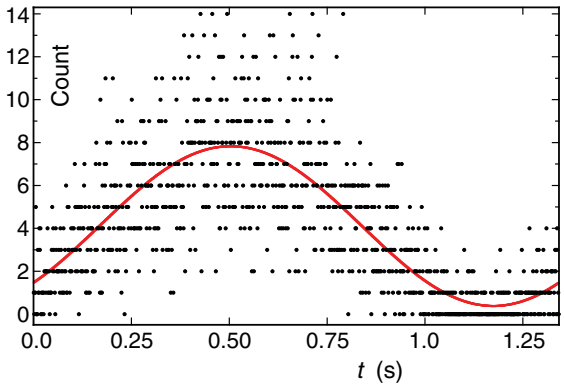

FIG. 8. Typical fringe data. Points denote counting data for 1024 counting intervals equally spaced over the fringe period $T = 1.3216$ s, with a total of 4206 counts. The solid curve shows the maximum-likelihood fit to an interference fringe having visibility $\mathcal{V} = 0.907$.

Interference was immediately apparent in the detected signal, yet the relative phase of the two beams appeared to drift, presumably due to slow length variations of the experimental paths. A typical phase drift was roughly π over 30 s. Thus a phase modulator was introduced into the attenuated pump light, which ramped its relative phase over the interval $[0, 2\pi]$ while the detector signal was recorded with a Stanford SR430 counter over 1024 temporal subintervals. The phase ramp was relatively rapid over a time $T = 1.3216$ s, the data were saved and analyzed in approximately 0.5 s, and the process was then repeated. One such data set is shown in Fig. 8, where a rise and fall of the local count rate is readily apparent, as could be expected for an interference fringe.

Auxiliary results had found that the recorded count appeared Poissonian, which motivates the following data treatment utilizing maximum likelihood principles [47]. Consider the count n_j of the jth time interval of Fig. 8. For optical intensity $I(t)$, n_j follows the Poisson distribution [48]

$$p(n_j) = e^{-\mu_j}\mu_j^{n_j}/n_j!, \tag{31}$$

with the mean of n_j given by

$$\mu_j = \eta \int_{t_j-\Delta t/2}^{t_j+\Delta t/2} I(t)dt, \tag{32}$$

where η is a constant characterizing the detector efficiency, t_j is the central time of the jth interval, and Δt is the interval width. Assuming statistical independence, the likelihood of all counts $\{n\}$ of a particular data set is given by the product of probabilities of the form of Eq. (31) as

$$p(\{n\}) = \prod_{j=1}^{1024} e^{-\mu_j} \mu_j^{n_j} / n_j!. \tag{33}$$

We now consider the intensity to be of the form $I(t) = I_\circ[1 + \mathcal{V}\cos(\frac{2\pi t}{T} + \phi)]$, where $\mathcal{V}$ and ϕ are, respectively, the fringe visibility and phase. To determine the best-fit fringe parameters, we find the maximum value of $p(\{n\})$ of Eq. (33) numerically, through variation of $\mathcal{V}$, ϕ, and $I_\circ$, with $\mathcal{V}$ and ϕ obviously being of principal interest. For the data of Fig. 8, we obtain $\mathcal{V} = 0.907$ and $\phi = -135°$; correcting the visibility for the measured constant background count of 217 s^{-1}, we obtain the corrected visibility as 0.976.

We produced a total of $N = 90$ such scans over approximately 3 min. The phase drifted as described earlier, but was otherwise of little interest. From the ensemble of scans, we compute the average background-corrected visibility as 0.961, with a standard deviation of $\sigma = 0.023$. We thus quote our corrected result as $\mathcal{V} = 0.961 \pm 0.002$, where the uncertainty is taken as $\sigma/\sqrt{N}$. In view of the noise apparent in Fig. 8, it may seem surprising that the experimental error quoted is small, but it should be kept in mind that the quoted visibility is based on the approximately 3.8×10^5 detected photons of the 90 scans. We thus conclude that these data exhibit an interference fringe of near-perfect visibility.

We have also studied the phase structure of the HG_{10} case of Fig. 6, whose two lobes are expected to be oppositely phased. Extending the previous method, we center the fiber in one lobe and record the detector signal as the attenuated pump phase was ramped. Then we center the fiber in the other lobe and repeat the phase ramp. The two data sets are taken approximately 2 s apart, so the phase drift between them is minimal. Such a data pair is shown in Figs. 9(a) and 9(b). The two data sets are again processed with the maximum-likelihood method to estimate the phase and visibility of each. In the example shown, the phase difference is thus estimated as $\Delta\phi = 191°$. In all, 45 pairs of such data were taken and the histogram of phase differences shown in Fig. 9(c) is seen to be centered near $\Delta\phi = 180°$. Averaging over the paired data, we report the phase difference as $177° \pm 2°$, where the uncertainty is obtained, as before, from the ensemble of results. Thus it is concluded that the two lobes are essentially antiphased.

The corrected visibilities were $\mathcal{V} = 0.880 \pm 0.005$ and $\mathcal{V} = 0.875 \pm 0.006$ in the two lobes; the reduction compared to the previous result was probably because of the additional alignment challenges that the HG_{10} mode presented. We also hasten to add that these measurements were preceded by a phase calibration procedure so as to compensate for contributions of wave-front tilt or any lack of orthogonality of the fiber scan. As described earlier, the HG_{10} pump beam was obtained from the phase-locked output of a Mach-Zehnder interferometer producing two oppositely phased circular Gaussian beams. To calibrate the phase, the interferometer was instead set to co-phase the two beams, which should produce a flat

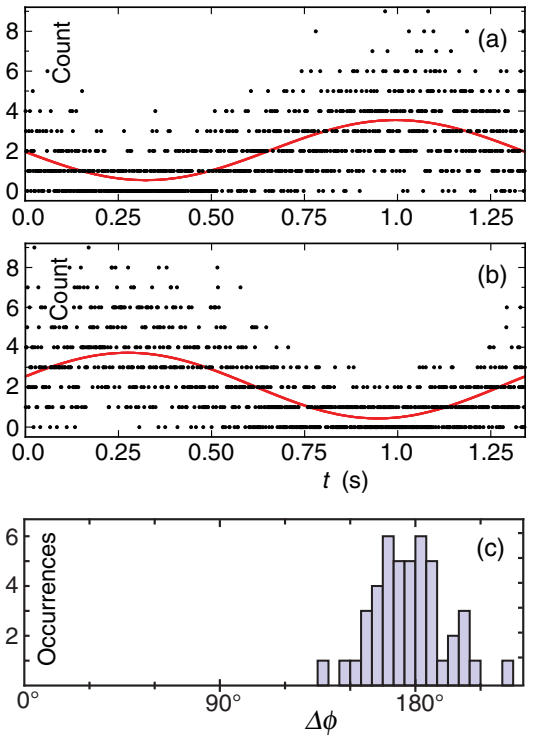

FIG. 9. (a) and (b) Points show experimental fringe data as in Fig. 8, but with the detector fiber centered in the left lobe of the HG_{10} intensity of Fig. 6 in (a) and then shifted to the right lobe in (b). Solid lines are maximum-likelihood fits to interference fringes, which here differ in phase by $\Delta\phi = 191°$. (c) Histogram of $\Delta\phi$ for 45 pairs of data, with an average $\Delta\phi$ of 177°.

phase across the pump beam waist. The up-converted beam was scanned with the fiber; the surface of constant phase was found to have a small tilt, which was removed here by scanning the fiber tip in the slightly tilted plane. At this point, the Mach-Zehnder was again set to antiphase the beams, and the procedure described earlier was begun, with the fiber scanned in the tilted plane.

In summary, it has been demonstrated that the up-converted light has essentially perfect mutual coherence with the pump. Fringes have been observed that are stable for times that are more than eight orders of magnitude greater than the reciprocal of the pump bandwidth. Further, significant evidence has been presented that the phase structure of beams is preserved, based on results with the HG_{10} pump beam.

IV. CONCLUSION

Here we have demonstrated effects of coherence being carried by SPDC. In particular, we have found that the original pump mode can be coherently reconstructed in the light up-converted by a second crystal. In theoretical work, this was proven directly from the mutual coherence function of the attenuated quantum pump and the up-converted amplitudes. In experiments, we have found that not only does the up-converted light resemble the pump mode, but we have observed that its interference with the attenuated pump can produce near-perfect fringe visibility. The theory predicts that the up-converted amplitude is linearly filtered by a far-field

transfer function that depends solely on the details of the nonlinear interactions; at a beam waist the effect amounts to a convolution with an amplitude point spread function. Such conceptually simple and intrinsically coherent results could not have been easily anticipated, particularly since the sole links between the input and output of our system are the pair states and vacuum fields of SPDC. Further, and from a broader perspective, the theoretical approach developed here may be used to provide exact solutions in other situations of interest where the multimodal character of fields is important and could be adapted to consider other quantum states of the original pump.

Our results may have implications for quantum information, since Eqs. (1) and (2) show that the pump mode may be viewed as encoded in the SPDC state. Our approach allows pump reconstruction only if the signal and idler channels have not been significantly tampered with; yet subtle modification of one channel could conceivably allow a desired effect to be produced in the up-converted amplitude. At the same time, our work has some unusual fundamental ramifications; for example, from basic principles, interference between the pump and up-converted light can occur with unit visibility only if the two contributing paths are indistinguishable [49,50]. Our work demonstrates the remarkable extremes under which this indistinguishability principle is valid; in one path, a pump photon is torn in two by vacuum fluctuations, leading to a continuum of photon pair and vacuum modes that travel through our optical system, with the process ultimately being reversed in another crystal. Yet, comparing this tortuous path to a second carrying nothing more than an attenuated pump beam, there is apparently no possible way to tell, even in principle, which path a photon has followed, and interference with perfect visibility is consequently obtained.

ACKNOWLEDGMENT

We are grateful for the support from the Consejo Nacional de Ciencia y Tecnología under Grant No. FON.INST./23/2016-189.

APPENDIX: QUANTUM STATE OF SPDC

Here we present a derivation of the SPDC state of Eqs. (1) and (2), with some associated results of general interest. The notation follows that introduced in Sec. II A. Similar studies have appeared previously [15,25,31]; however, our approach differs because we employ a quantized pump having a continuum of spatiotemporal modes. This is an accurate representation of our experimental situation and is also important to our proof of mutual coherence in Sec. II A. A second difference is that our approach will lead to expressions for commonly measured quantities on *absolute* scales, which is of considerable general utility.

We start with the pump, which we take to be in a coherent state. The representation employed is related to the continuum coherent states in frequency that have been discussed elsewhere [34]; here they are extended to consider a continuum of pump wave vectors as follows. The pump state $|\{\psi_p\}\rangle$ is defined by the eigenvalue equation

$$\hat{a}(\mathbf{k}_p)|\{\psi_p\}\rangle = \sqrt{N_p}\psi_p(\mathbf{k}_p)e^{i\Phi_p}|\{\psi_p\}\rangle, \tag{A1}$$

where $\psi_p(\mathbf{k}_p)$ is a weighting function, Φ_p is the pump phase, and

$$N_p = \int d\mathbf{k}_p \langle\{\psi_p\}|\hat{a}^\dagger(\mathbf{k}_p)\hat{a}(\mathbf{k}_p)|\{\psi_p\}\rangle \tag{A2}$$

is the mean number of pump photons in a time Δt, which is much longer than an optical period. The usual normalization condition $\langle\{\psi_p\}|\{\psi_p\}\rangle = 1$, when combined with Eqs. (A1) and (A2), implies that $\psi_p(\mathbf{k}_p)$ is normalized as

$$\int d\mathbf{k}_p |\psi_p(\mathbf{k}_p)|^2 = 1. \tag{A3}$$

In the following analysis, when transforming integration variables from $\mathbf{k}_p$ to $(\omega_p, \theta_p, \phi_p)$, we consider $\psi(\mathbf{k}_p)$ to be the product of a spectral function and an angular amplitude spectrum as $\psi_p(\mathbf{k}_p) = \frac{\mathcal{A}(\omega_p)}{\sqrt{\eta_p k_p}}\mathcal{F}(\theta_p, \phi_p|\omega_p)$, where Eq. (A3) is satisfied by requiring that

$$\int d\omega_p |\mathcal{A}(\omega_p)|^2 = 1 \tag{A4}$$

and that, for all ω_p,

$$\iint d\theta_p d\phi_p \sin\theta_p |\mathcal{F}(\theta_p, \phi_p|\omega_p)|^2 = 1. \tag{A5}$$

Should the pump state $|\{\psi_p\}\rangle$ be attenuated to the point that the probability of it containing more than one photon can be neglected, it may be written as [51]

$$|\{\psi_p\}\rangle = \left[\hat{I} + \gamma\sqrt{N_p}\int d\mathbf{k}_p \psi_p(\mathbf{k}_p)e^{i\Phi_p}\hat{a}^\dagger(\mathbf{k}_p)\right]|\text{vac}\rangle, \tag{A6}$$

where γ is the attenuation factor, with $|\gamma| \ll 1$. Equation (A6) is employed solely in calculating the mutual coherence in Eq. (17), while the unattenuated pump state defined by Eq. (A1) is employed in the development that follows below.

The down-converted state may be found from first-order perturbation theory as in Eq. (6), but with different input and output states as

$$|\psi_{\text{SPDC}}\rangle = \left[\hat{I} - \frac{i}{\hbar}\int_{-\infty}^{\infty} dt\, \hat{H}_{\text{int}}(t)\right]|\{\psi_p\}\rangle. \tag{A7}$$

The interaction Hamiltonian is given by Eq. (7), whose Hermitian conjugate term is here the relevant term. The spatial and temporal integrations arising from Eqs. (7) and (A7) are performed with the same assumptions used to derive Eq. (9). After removing the pump state, the down-converted state follows as

$$|\psi_{\text{SPDC}}\rangle = \left[\hat{I} - \sqrt{\frac{N_p d_{\text{eff}}^2 L^2 \hbar}{16\pi^3\epsilon_0 c^3}}\int d\mathbf{k}_p \int_{\mathcal{D}_s} d\mathbf{k}_s \int_{\mathcal{D}_i} d\mathbf{k}_i \times \sqrt{\frac{\omega_p\omega_s\omega_i}{n_p n_s n_i \eta_p \eta_s \eta_i}}\delta(\omega_p - \omega_s - \omega_i)\delta\left(\Delta k_x^d\right)\delta\left(\Delta k_y^d\right) \times \psi(\mathbf{k}_p)e^{i\Phi_p}s(\Delta k_z)\hat{a}^\dagger(\mathbf{k}_s)\hat{a}^\dagger(\mathbf{k}_i)\right]|\text{vac}\rangle. \tag{A8}$$

The differential $d\mathbf{k}_p$ is then expanded as $d\omega_p d\theta_p d\phi_p k_p^2 \eta_p \sin\theta_p$ and the ω_p integration is done using the frequency δ function, which sets $\omega_p = \omega_s + \omega_i$. The

angular integrations are performed using the identity that, for an arbitrary function $f(\theta_p, \phi_p)$,

$$\iint d\theta_p d\phi_p \sin\theta_p f(\theta_p, \phi_p)\delta\left(\Delta k_x^d\right)\delta\left(\Delta k_y^d\right) = \frac{f\left(\theta_p^{\rm o}, \phi_p^{\rm o}\right)}{k_p^2 \cos\theta_p^{\rm o}}, \tag{A9}$$

where $\phi_p^{\rm o}$ and $\theta_p^{\rm o}$ are found from, respectively, Eqs. (4) and (5). The down-converted state is then

$$|\psi_{\rm SPDC}\rangle = \left[\hat{I} - \int d\mathbf{k}_s \int d\mathbf{k}_i \psi(\mathbf{k}_s, \mathbf{k}_i)\hat{a}^\dagger(\mathbf{k}_s)\hat{a}^\dagger(\mathbf{k}_i)\right]|{\rm vac}\rangle, \tag{A10}$$

where the two-photon amplitude $\psi(\mathbf{k}_s, \mathbf{k}_i)$ is given by

$$\psi(\mathbf{k}_s, \mathbf{k}_i) = \sqrt{\frac{N_p d_{\rm eff}^2 L^2 \hbar\omega_p\omega_s\omega_i\eta_p^+}{16\pi^3\epsilon_0 c^3 n_p^+ n_s n_i \eta_s \eta_i}} \frac{\psi_p(\mathbf{k}_p^+)e^{i\Phi_p}}{\cos\theta_p^{\rm o}} s\left(\Delta k_z^d\right), \tag{A11}$$

which is Eq. (2) of Sec. II A and where n_p^+, η_p^+, and $\mathbf{k}_p^+$ are defined as they were following Eq. (2). The state representation of Eqs. (A10) and (A11) has a form that is typical of other works; however, it will be seen that our expressions here lead to results on absolute scales.

While the equations presented above are those necessary in Sec. II A, we now present a few general results that follow from $\psi(\mathbf{k}_s, \mathbf{k}_i)$. The rate R_π of coincident detected photon pairs may be calculated with an approach described elsewhere [15], in which the usual detection conditions are assumed (the integration time is much longer than the reciprocal of the detected bandwidth). For $\psi(\mathbf{k}_s, \mathbf{k}_i)$ from Eq. (A11), this leads directly to

$$R_\pi = 2\beta c^2 F_p \int_{\mathcal{D}_s} d\mathbf{k}_s \int_{\mathcal{D}_i} d\mathbf{k}_i \frac{\hbar\omega_p\omega_s\omega_i}{n_p n_s n_i \eta_s \eta_i} \times \frac{|\mathcal{A}(\omega_p)|^2}{k_p^{+2}\cos^2\theta_p^{\rm o}} \left|\mathcal{F}\left(\theta_p^{\rm o}, \phi_p^{\rm o}|\omega_p\right)\right|^2 |s(\Delta k_z)|^2, \tag{A12}$$

where $\beta = \frac{d_{\rm eff}^2 L^2}{16\pi^3\epsilon_0 c^5}$, $F_p = N_p/\Delta t$, and $\mathcal{D}_s$ and $\mathcal{D}_i$ represent the integration parameters of, respectively, the signal and idler detectors; further, as is the usual experimental case with two distinct detectors, it has now been assumed that there is no overlap between $\mathcal{D}_s$ and $\mathcal{D}_i$ in $\mathbf{k}$ space. We have previously presented numerical evaluations of a similar (albeit unnormalized) expression, compared with experimental observations [52].

In the narrow-band pump limit we have that $|\mathcal{A}(\omega_p)|^2 \to \delta(\omega_p - \omega_p^{\rm o})$. The idler frequency integration in Eq. (A12) may then be performed and R_π becomes

$$R_\pi = 2\beta c^2 F_p \hbar\omega_p^{\rm o} \int_{\mathcal{D}_s} d\mathbf{k}_s \iint_{\Delta\Omega_i} d\theta_i d\phi_i \frac{\omega_s\omega_i}{n_p n_s n_i \eta_s} \times \frac{k_i^2 \sin\theta_i}{k_p^{+2}\cos^2\theta_p^{\rm o}} \left|\mathcal{F}\left(\theta_p^{\rm o}, \phi_p^{\rm o}|\omega_p^{\rm o}\right)\right|^2 |s(\Delta k_z)|^2 T_i(\omega_i), \tag{A13}$$

with $\omega_i = \omega_p^{\rm o} - \omega_s$ and where, for the idler detector, $\Delta\Omega_i$ is its collection angle and $T_i(\omega_i)$ is its filter transmission function. Since experiments are often performed with narrow-band pump conditions, Eq. (A13) is commonly useful. Further, in the wide-pump limit we have that $|\mathcal{F}(\theta_p^{\rm o}, \phi_p^{\rm o}|\omega_p^{\rm o})|^2 \to \delta(k_p^+ \sin\theta_p^{\rm o}\cos\phi_p^{\rm o})\delta(k_p^+ \sin\theta_p^{\rm o}\sin\phi_p^{\rm o}) = \delta(k_{s,x} + k_{i,x})\delta(k_{s,y} + k_{i,y})$, where we have used the condition $\Delta\mathbf{k}^d = 0$ that established Eqs. (4) and (5) to write the arguments of the δ functions in terms of signal and idler variables. We then perform the idler angular integrations in a manner analogous to Eq. (10), with the result

$$R_\pi = 2\beta F_p \hbar\omega_p^{\rm o} \int d\omega_s \frac{\omega_s^3\omega_i n_s}{n_p n_i} T_s(\omega_s)T_i(\omega_i) \times \iint_{\Delta\Omega_s} d\theta_s d\phi_s \frac{\sin\theta_s}{\cos\theta_i} |s(\Delta k_z)|^2 D_i(\theta_i, \phi_i), \tag{A14}$$

where θ_i follows from $n_i\omega_i \sin\theta_i = n_s\omega_s \sin\theta_s$. We emphasize that Eqs. (A12)–(A14) predict absolute pair rates for given experimental conditions.

We now consider the signal photon rate R_s passing through a circular aperture of angular radius $\tilde{\theta}_c$, without bandwidth filtering and without restrictions on the idler mode. This follows from Eq. (A14) with $D_i(\theta_i, \phi_i) = 1$ and $T_\epsilon(\omega_\epsilon) = 1$ for $\epsilon \in \{s, i\}$. Integrating ϕ_s trivially over $[0, \pi]$, we obtain

$$R_s = 2\pi\beta F_p \hbar\omega_p^{\rm o} \int d\omega_s \frac{\omega_s^3\omega_i n_s}{n_p n_i} \int_0^{\Theta_s} d\theta_s \frac{\sin\theta_s}{\cos\theta_i} |s(\Delta k_z)|^2, \tag{A15}$$

where $\Theta_s = \arcsin[\sin\tilde{\theta}_c/n_s]$. By changing the integration variables of Eq. (A15) from ω_s to $\omega_i = \omega_p^{\rm o} - \omega_s$ and from θ_s to its phase-matched idler angle θ_i, an expression is obtained that is identical to Eq. (A15), but with signal and idler variables interchanged. This implies that $R_i = R_s$, which must be the case from physical symmetry, and the total photon rate follows as $R = R_s + R_i = 2R_s$.

The power of the signal light P_s follows from an expression analogous to Eq. (A15) as

$$P_s = 2\pi\beta P_p \int d\omega_s \frac{\hbar\omega_s^4\omega_i n_s}{n_p n_i} \int_0^{\Theta_s} d\theta_s \frac{\sin\theta_s}{\cos\theta_i} |s(\Delta k_z)|^2, \tag{A16}$$

where $P_p = F_p\hbar\omega_p^{\rm o}$. The integrand of Eq. (A16) differs by a factor of $(4\cos\theta_i)^{-1}$ upon comparison with a previous result [53]; however, we note that our $(\cos\theta_i)^{-1}$ factor is essential in obtaining the correct functional symmetry discussed in relation to Eq. (A15). Finally, the total SPDC power in the aperture is given by $P = P_s + P_i = 2P_s$.

[1] X. Y. Zou, L. J. Wang, and L. Mandel, Phys. Rev. Lett. **67**, 318 (1991).

[2] L. J. Wang, X. Y. Zou, and L. Mandel, Phys. Rev. A **44**, 4614 (1991).

[3] Z. Y. Ou, L. J. Wang, and L. Mandel, Phys. Rev. A **40**, 1428 (1989).

[4] Z. Y. Ou, L. J. Wang, X. Y. Zou, and L. Mandel, Phys. Rev. A **41**, 566 (1990).

[5] A. V. Burlakov, M. V. Chekhova, D. N. Klyshko, S. P. Kulik, A. N. Penin, Y. H. Shih, and D. V. Strekalov, Phys. Rev. A **56**, 3214 (1997).

[6] A. Heuer, S. Raabe, and R. Menzel, Phys. Rev. A **90**, 045803 (2014).

[7] A. Heuer, R. Menzel, and P. W. Milonni, Phys. Rev. Lett. **114**, 053601 (2015).

[8] A. Heuer, R. Menzel, and P. W. Milonni, Phys. Rev. A **92**, 033834 (2015).

[9] R. Menzel, A. Heuer, and P. W. Milonni, arXiv:1705.06030.

[10] G. B. Lemos, V. Borish, G. D. Cole, S. Ramelow, R. Lapkiewicz, and A. Zeilinger, Nature (London) **512**, 409 (2014).

[11] D. A. Kalashnikov, A. V. Paterova, S. P. Kulik, and L. A. Krivitsky, Nat. Photon. **10**, 98 (2016).

[12] M. V. Chekhova and Z. Y. Ou, Adv. Opt. Photon. **8**, 104 (2016).

[13] M. I. Kolobov, E. Giese, S. Lemieux, R. Fickler, and R. W. Boyd, J. Opt. **19**, 054003 (2017).

[14] A. V. Paterova, H. Yang, C. An, D. A. Kalashnikov, and L. A. Krivitsky, Quantum Sci. Technol. **3**, 025008 (2018).

[15] A. Joobeur, B. E. A. Saleh, T. S. Larchuk, and M. C. Teich, Phys. Rev. A **53**, 4360 (1996).

[16] B. Dayan, A. Pe'er, A. A. Friesem, and Y. Silberberg, Phys. Rev. Lett. **94**, 043602 (2005).

[17] A. Pe'er, B. Dayan, A. A. Friesem, and Y. Silberberg, Phys. Rev. Lett. **94**, 073601 (2005).

[18] K. A. O'Donnell and A. B. U'Ren, Phys. Rev. Lett. **103**, 123602 (2009).

[19] K. A. O'Donnell, Phys. Rev. Lett. **106**, 063601 (2011).

[20] K. A. O'Donnell and V. G. Garces, J. Mod. Opt. **62**, 1616 (2015).

[21] J. M. Lukens, A. Dezfooliyan, C. Langrock, M. M. Fejer, D. E. Leaird, and A. M. Weiner, Phys. Rev. Lett. **111**, 193603 (2013).

[22] J. M. Lukens, A. Dezfooliyan, C. Langrock, M. M. Fejer, D. E. Leaird, and A. M. Weiner, Phys. Rev. Lett. **112**, 133602 (2014).

[23] O. D. Odele, J. M. Lukens, J. A. Jaramillo-Villegas, C. Langrock, M. M. Fejer, D. E. Leaird, and A. M. Weiner, Opt. Express **23**, 21857 (2015).

[24] A. Gatti, E. Brambilla, and L. Lugiato, in *Progress in Optics*, edited by E. Wolf (Elsevier, Amsterdam, 2008), Vol. 51, p. 251.

[25] M. Hamar, J. Peřina Jr., O. Haderka, and V. Michálek, Phys. Rev. A **81**, 043827 (2010).

[26] A. Joobeur, B. E. A. Saleh, and M. C. Teich, Phys. Rev. A **50**, 3349 (1994).

[27] S. E. Harris, Phys. Rev. Lett. **98**, 063602 (2007).

[28] B. Dayan, Phys. Rev. A **76**, 043813 (2007).

[29] B. R. Holstein, *Topics in Advanced Quantum Mechanics* (Addison-Wesley, Reading, 1992).

[30] M. H. Rubin, D. N. Klyshko, Y. H. Shih, and A. V. Sergienko, Phys. Rev. A **50**, 5122 (1994).

[31] C. K. Hong and L. Mandel, Phys. Rev. A **31**, 2409 (1985).

[32] Y. H. Shih, Rep. Prog. Phys. **66**, 1009 (2003).

[33] M. M. Fejer, G. A. Magel, D. H. Jundt, and R. L. Byer, IEEE J. Quantum Electron. **28**, 2631 (1992).

[34] K. J. Blow, R. Loudon, S. J. D. Phoenix, and T. J. Shepherd, Phys. Rev. A **42**, 4102 (1990).

[35] B. Huttner and S. M. Barnett, Phys. Rev. A **46**, 4306 (1992).

[36] A. Lukš and V. Peřinová, *Quantum Aspects of Light Propagation* (Springer, Berlin, 2009).

[37] L. G. Helt, M. J. Steel, and J. E. Sipe, New J. Phys. **17**, 013055 (2015).

[38] L. G. Helt and M. J. Steel, Opt. Lett. **40**, 1460 (2017).

[39] L. Mandel, Phys. Rev. **159**, 1084 (1967).

[40] D. E. Zelmon, D. L. Small, and D. Jundt, J. Opt. Soc. Am. B **14**, 3319 (1997).

[41] H. Y. Shen, H. Xu, Z. D. Zeng, W. X. Lin, R. F. Wu, and G. F. Xu, Appl. Opt. **31**, 6695 (1992).

[42] J. W. Goodman, *Introduction to Fourier Optics*, 3rd ed. (Roberts, Englewood, 2005).

[43] S. Lerch, B. Bessire, C. Bernhard, T. Feurer, and A. Stefanov, J. Opt. Soc. Am. B **30**, 953 (2013).

[44] E.-G. Neumann, *Single-Mode Fibers: Fundamentals* (Springer, Berlin, 1988), Sec. 7.2.1.

[45] D. V. Petrov, F. Canal, and L. Torner, Opt. Commun. **143**, 265 (1997).

[46] M. W. Beijersbergen, L. Allen, H. E. L. O. van der Veen, and J. P. Woerdman, Opt. Commun. **96**, 123 (1992).

[47] A. Papoulis and S. U. Pillai, *Probability, Random Variables, and Stochastic Processes*, 4th ed. (McGraw-Hill, New York, 2002).

[48] L. Mandel and E. Wolf, *Optical Coherence and Quantum Optics* (Cambridge University Press, Cambridge, 1995), Sec. 9.5.

[49] L. Mandel, Opt. Lett. **16**, 1882 (1991).

[50] B.-G. Englert, Phys. Rev. Lett. **77**, 2154 (1996).

[51] R. J. Glauber, Phys. Rev. **131**, 2766 (1963).

[52] G. D. Jimenez, V. G. Garces, and K. A. O'Donnell, Phys. Rev. A **96**, 023828 (2017).

[53] R. L. Byer and S. E. Harris, Phys. Rev. **168**, 1064 (1968).